Engineering Porous Biochar for Electrochemical Energy Storage

Cheikh Ahmadou Bamba Diop , Déthié Faye , Momath Lo * , Dahbia Bakiri , Huifeng Wang , Mohamed El Garah , Vaishali Sharma , Aman Mahajan , Mohamed Jouini , Diariatou Gningue-Sall , Mohamed Mehdi Chehimi *

Posted Date: 29 September 2025

doi: 10.20944/preprints202509.2454.v1

Keywords: *Pennisetum glaucum*; biochar; porous materials; electrode materials; supercapacitor; capacitive retention

 doi:10.20944/preprints202509.2454.v1

Article

Engineering Porous Biochar for Electrochemical Energy Storage

Cheikh Ahmadou Bamba Diop [1,2], Déthié Faye [1], Momath Lo [1,*], Dahbia Bakiri [2,3], Huifeng Wang [2], Mohamed El Garah [4], Vaishali Sharma [5], Aman Mahajan [5], Mohamed Jouini [2], Diariatou Gningue-Sall [1] and Mohamed Mehdi Chehimi [2,*]

[1] Laboratoire de Chimie Physique Organique et d'Analyses Environnementales (LCPOAE), Département de Chimie, Faculté des Sciences et Techniques, Université Cheikh Anta Diop, Dakar, Sénégal

[2] Université Paris Cité, CNRS, ITODYS (UMR 7086), Paris 75013, France

[3] Iut de Paris-Pajol-Université Paris Cité, Paris 75018, France

[4] LASMIS, Pôle Technologique de Sud – Champagne, Antenne de Nogent – 52, Nogent, 52800, France

[5] Guru Nanak Dev University (GNDU), Amritsar, Punjab, India

* Correspondence: momath.lo@ucad.edu.sn (M.L.); mohamed.chehimi@cnrs.fr (M.M.C.)

Abstract

In recent years, porous carbon-based materials have demonstrated their potential as electrode materials, particularly as supercapacitors for energy storage. The specific capacity of a carbon-based material is strongly influenced by its porosity. Herein, activated biochar (BCA) from millet was prepared using $ZnCl_2$ as an activator at temperatures of 400, 700, and 900 °C. Activation was achieved through wet and dry impregnation of millet bran powder particles. The porosity of BCAs was assessed by determining the iodine and methylene blue numbers (N_I and N_{MB}, respectively), which provide information on microporosity and mesoporosity, respectively. Characterization of the BCAs was carried out using Raman spectroscopy, X-ray diffraction, X-ray photoelectron spectroscopy, and cyclic voltammetry. The data show that the BCA prepared at 700 °C following dry impregnation, P700(p), has the highest N_I and the highest geometric mean value ($\tilde{n} = \sqrt{N_I \times N_{MB}}$), a descriptor we introduce to characterize the overall porosity of the biochars. P700(p) biochar exhibited remarkable electrochemical properties and a maximum specific capacitance of 440 $F.g^{-1}$ at a current density of 0.5 A/g. These performances are best correlated with $\tilde{n}$. Moreover, the capacitive retention increases with cycling, up to 130%, thus suggesting electrochemical activation of the biochar during the galvanostatic charge-discharge process. To sum up, the combination of pyrolysis temperature and the method of impregnation permitted to obtaining a porous biochar with excellent electrochemical properties, meeting the requirements of supercapacitors and batteries.

Keywords: *Pennisetum glaucum*; biochar; porous materials; electrode materials; supercapacitor; capacitive retention

Introduction

As the world's population continues to grow, increasing energy demand is becoming a growing concern. For some time, energy has been derived almost entirely from fossil fuels, which are non-renewable and generate CO_2 emissions. These harmful gases pose a risk to living beings and their environment. Today, studies are focusing on renewable and ecological energies; they are inexhaustible and accessible [1,2]. Nevertheless, their sporadic nature poses a real challenge to researchers. Consequently, the development of systems capable of converting and conserving energy while preserving the environment remains a challenge. With this in mind, supercapacitors or electrochemical capacitors, whose main aim is to store as many ions as possible in the form of charge, are the materials of choice. They are characterized by high power density and high energy density. They possess characteristics such as conductivity and porosity, as well as a large active surface area

 doi:10.20944/preprints202509.2454.v1

[3]. There are two primary types of supercapacitors, distinguished by their charge storage methods: electrochemical double-layer capacitors (EDLCs) and pseudocapacitors. EDLCs store energy through interactions at the electrode surface with ions in the electrolyte, without any chemical reaction. The ions deposit on the surface, forming a layer that can accumulate charges. Electrochemically, they are characterized by rectangular voltamograms. Pseudocapacitors store energy through reversible redox reactions between the electrolyte and electroactive species on the electrode surface, which involve electron transfer during these reactions. They exhibit rectangular voltamograms with inflection points [4,5]. The most commonly used capacitor electrode materials are made of carbon, including carbon itself, fullerenes, carbon nanotubes, graphene, and carbon aerogel. They are good conductors and typically have a large surface area and surface pores, making carbon an ideal material for a capacitor [6]. However, these materials are expensive and have limitations, such as fullerene's low surface area or graphene's tendency to clump together easily, which restricts their performance. Recently, biochar-based electrodes raised much interest due to their properties that suit charge storage [7–9]. Biochars are produced from the carbonization of the biomass in an anaerobic or anoxic environment. They are highly carbon-rich materials, often porous due to the thermochemical conversion of the lignocellulosic matter which releases mainly H, N, and O-containing species [10,11]. They are available in large quantities and have the potential to replace other carbon allotropes [12,13]. Biochars meet capacitor criteria because of their porous structure and the possibility to modify their chemical composition by adsorption, grafting or decoration with nanoparticles [14–17]. The characteristics of biochar depend entirely on surface and interface properties. These characteristics are influenced by factors such as the type of biomass used, temperature, and residence time [18]. Furthermore, biochar in its natural form may exhibit limited activity due to its low porosity and smaller active surface area. Additional activation or treatment can enhance its performance [19]. Activation of biochar mainly improves catalytic performance and increases the number of catalytic sites [20], generally manifested by a change in its surface texture [21]. However, the need for metal salt additives, which provide biochar with mechanical strength, affects the design of electrode materials and compromises electrode durability during recycling [22]. The use of $ZnCl_2$-activated biochar is investigated as a potential approach for fabricating electrodes for supercapacitors [23]. Observations validated a lower internal resistance and a device elaborated with a higher mesoporosity level and at a homogeneous matrix distribution. Areal capacitance of $ZnCl_2$-activated biochar electrodes reached 342 $mF.cm^{-2}$, which promotes the interplay of double-layer electrical capacitance/pseudocapacitance mechanisms in a matrix that favors electrolyte interactions in the pores. Micropores (ultramicropores) and mesopores are true sites of charge capture in the form of energy [24]. To better distinguish pores, iodine and methylene blue numbers are determined. The degree of porosity, confirmed by BET measurements, is directly associated with the iodine value [25].

Evaluation of these two criteria provides data on the porosity of the various biochars. Due to their respective dimensions, the iodine index (N_I) focuses more on microporosity while the methylene blue index (N_{MB}) focuses on mesoporosity [26,27]. A review of the literature reveals a lack of correlation between the capacity of biochar electrode materials and the N_I and N_{MB} descriptors.

In this study, millet bran, a waste product collected during the processing of Senegalese millet, is selected as biomass. Millet is rich in minerals, and considered the second most consumed food in Senegal, just after rice. Its production was estimated to be 900,000-1,000,000 tons in 2021 [9]. The biochars were prepared by co-pyrolysis of the biomass and $ZnCl_2$ activator at a mass ratio of 1:2, through dry and wet impregnation procedures. The activated biochar samples were characterized by XRD, SEM, XPS, and Raman. Their porosity was probed with iodine and methylene blue. The biochars served as electrode materials and were characterized by cyclic voltammetry and electrochemical impedance spectroscopy. They were then subjected to galvanostatic discharge charge (GCD) to assess their propensity to serve as supercapacitors. Not only is it demonstrated that the specific capacity could be high and tuned by combining activation and pyrolysis temperature, but also the electrochemical performances could be correlated with a new physicochemical descriptor

 doi:10.20944/preprints202509.2454.v1

calculated as the geometric mean value of N_I and N_{MB} numbers. Such a correlation has not been reported so far, hence the interest of the actual investigation.

2. Experimental

2.1. Reagents and Instrumentation

Methylene blue ($C_{16}H_{18}ClN_3S$) ≥ 97%, iodine (I_2) ≥ 99.8%, potassium iodide (KI) ≥ 99.5%,

Nafion ($C_7HF_{13}O_5S.C_2F_4$) 5 %, ethanol (C_2H_6O) 99% and sulfuric acid (H_2SO_4) 99% Sigma-Aldrich. Millet bran residue of millet from Senegal (Thies/Mbour) was the biomass feedstock.

Iodine and methylene blue numbers are measured to characterize the pores. An HR800 spectrometer with a 633 nm laser is used to produce the Raman spectrum, and a diffractometer with an XPERT-PRO system is used to obtain the XRD spectra. A K Alpha+ apparatus (Thermo) equipped with a flood gun to counteract the build-up of static charges and a monochromated X-ray source (Al Kα, hv = 1486.6 eV) was used for XPS measurements. The data processing was performed using Avantage software, version 6.8.0. A Hitachi SU-8030 machine was used to acquire SEM images.

Electrochemical experiments were carried out on an SP-150 Biologic potentiostat/galvanostat. The glass cell has three electrodes: a saturated Ag/AgCl reference electrode, a graphite counter electrode, and a GC working electrode (diameter D = 3 mm and apparent surface S = 14.137 mm^2).

2.2. Synthesis of Actived Biochar

Activated biochar was prepared via two routes: wet and dry impregnation. (i) The first method consists in impregnating 1g of biomass in a beaker containing a ZnCl2 solution (2g of salt in 10 mL of water). The wet biomass powder is covered with with perforated aluminum foil and left to dry at 105 ° C for 24 hours. (ii) The second method involves dry impregnation (p), consisting in mixing 2 g of $ZnCl_2$ and 1 g of biomass. The samples were pyrolyzed at 400, 700, and 900 °C for 1 hour under nitrogen. After pyrolysis, the biochars were washed with HCl to remove traces of zinc chloride, metallic zinc, or zinc oxide, and then with distilled water to remove chlorides. The active biochars were dried at 105 °C for 24 hours.

2.3. Determination of Iodine and Methylene Blue Numbers

The quantity of iodine (in milligrams) absorbed is the iodine number N_I, permits to characterize the activity of carbonaceous materials [28]. In brief, an iodine solution is prepared by adding 62.25 mg KI to a beaker and 31.75 mg of I_2. The mixture is stirred for 24 hours in a dark place to facilitate dissolution. The dissolved solution is transferred to a 500 mL volumetric flask. 5 mg of biochar is placed in a beaker, and 10 mL of 5% hydrochloric acid is added. The mixture is boiled for 30 seconds, then cooled to room temperature before adding 100 mL of the prepared iodine solution and stirring for 15 minutes. 10 mL were pipetted with a syringe and filtered to remove the biochar, then the amount of iodine adsorbed by the biochar was determined by UV-Visible.

The methylene blue index N_{MB} represents the amount of MB consumed by 1 g of adsorbent. It is measured by preparing a stock solution of 100 $mg.L^{-1}$ of MB. This solution is diluted to give a daughter solution of 50 $mg.L^{-1}$. 100 mL of the daughter solution is taken and placed in a beaker containing 40 mg biochar. The mixture is stirred at 120 rpm for 1 h. The quantity of adsorbed MB is measured using the same protocol as for the iodine value.

The adsorption index N (adsorption capacity C) is calculated using:

$$C = \frac{C_0 - C_e}{m} \times V \quad (1)$$

C_0: initial concentration ($mg.L^{-1}$), C_e: final concentration ($mg.L^{-1}$), V: volume of aqueous solution (L), and m: weight of biochars (g).

2.4. Electrochemical Properties of Biochar

 doi:10.20944/preprints202509.2454.v1

The working electrode was polished, cleaned, and rinsed before any electrochemical measurements. This treatment process is as follows: alumina powder (diameter 0.05µm) is used for abrasive polishing as the first step in preparing the glassy carbon (GC) electrode, which ensures thorough and effective regeneration of the electrode surface. To ensure there are no contaminants on the electrode surface, the second step involves immersing the electrode in a solution of 10 mL of H_2SO_4 (0.5M) and performing cyclic voltammetry for ten cycles within a potential range of 0 to 0.8V.

Biochar inks, created by mixing 5 mg of biochar with 1 mL of ethanol containing 10 µL of Nafion, were used to modify the GC working electrode. To turn the suspension into ink, the mixture was placed in an ultrasonic bath for 30 minutes. Then, 4 µL of the ink was applied onto the surface of the well-polished GC electrode and let it air dry for hours, heated [29]. After drying, the resulting working electrode was used for electrochemical measurements.

CV analyses were recorded between 0 and 0.8 V/Ag/AgCl in an aqueous solution of 0.5 M sulfuric acid. The active surface area of biochar compounds was determined using the Randles-Sevcik equation (2):

$$I_P = (2.69 \times 10^5)\, n^{\frac{3}{2}} \times A \times D^{\frac{1}{2}} \times V^{\frac{1}{2}} \times C_0 \quad (2)\ [30]$$

Ip: anodic current, Co: electrolyte concentration, V: scan speed, n: number of electrons transferred, and D: diffusion coefficient of the species involved. In a solution of sulfuric acid, H_2SO_4, n=2 and $D=1.8\times10^{-5}$.

The specific capacity (Cs) of hydro/biochar is determined from the voltammograms by using the following equation [31,32].

$$C_S = \frac{\int I dV}{v \times m \times \Delta V} \quad (3)$$

I: the response current, V: the corresponding potential, m: the mass of the material deposited on the surface of the electrode, ΔV: potential window, and v: the scanning speed (mV/S).

Electrochemical impedance spectroscopy (EIS) of the biochars was also recorded in a frequency range of 0.1 Hz to 200 kHz. Galvanostatic charge-discharge (GCD) measurements were also performed in the same potential range as the CVs, at current densities from 0.5 to 5 A g^{-1}. The specific capacity Csp ($F.g^{-1}$) was calculated from the discharge portion of the GCD curve using equation (3): $C_{sp} = \frac{I\Delta t}{m\Delta V}$ (4)

$$E = \frac{1}{2} CV^2 \quad (5)$$

$$P = \frac{E}{\Delta t} \quad (6)$$

Csp: specific capacitance ($F.g^{-1}$); I: applied current (A); Δt: discharge time (s); m: mass of active material (g); ΔV: potential window (V); E: energy density ($Wh.kg^{-1}$) and P: power density ($W.kg^{-1}$).

3. Results and Discussion

3.1. Morphology of the Biochar Powder Particles

Figure 1 shows SEM images of BCAs obtained at different pyrolysis temperatures. The images show rough surfaces for all samples. At 400 °C, for all types of impregnation, the pores are negligible, indicating that the activator melting bridge has not been reached. These results show that $ZnCl_2$ melts and forms bubbles during the cooling phase, which stick to the surface of the biochar, obstructing the pores [33]. Activated biochars P700(p), P700(aq), and P900(p) feature pores that would result from the thermal transformation of $ZnCl_2$, followed by the release of gases (HCl, CO_2, CO, and/or Zn). At temperatures above the melting point, $ZnCl_2$ decomposes and accelerates the volatilization of organic matter, leaving voids or pores [34]. However, in the case of P900(aq), the material begins to degrade and the pores gradually disappear, which may be due to the effect of temperature and the type of impregnation. This shows that dry impregnation offers well-developed porosity for P700(p) and P900(p) materials compared to those prepared by wet impregnation, whose pores appear clogged, for example P700(aq), or are destroyed in the case of P900(aq).

 doi:10.20944/preprints202509.2454.v1

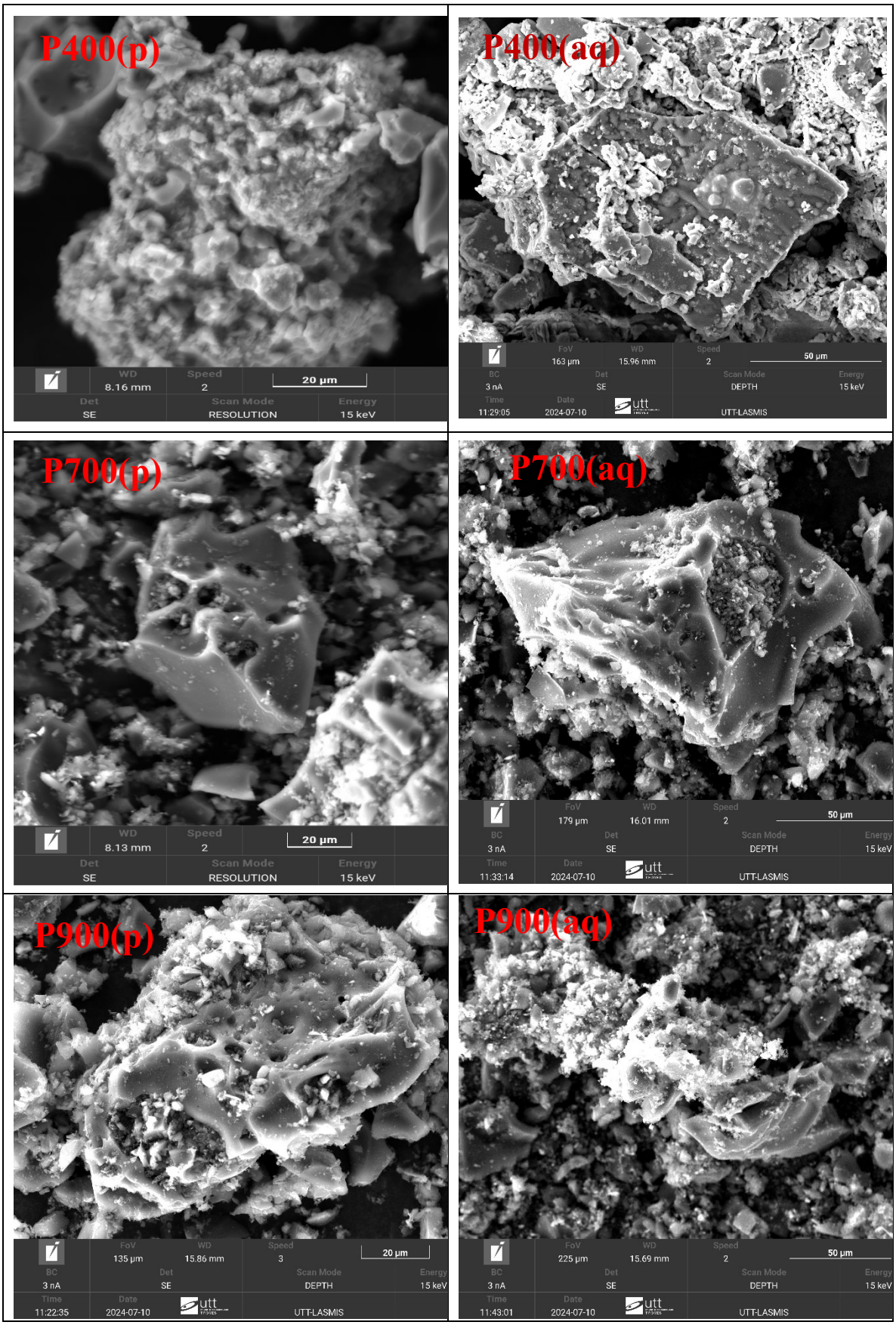

Figure 1. SEM images of biochar samples prepared by wet (aq) and dry (p) impregnation with $ZnCl_2$, at 400, 700 and 900 °C.

3.2. XDR Analysis

 doi:10.20944/preprints202509.2454.v1

Figure 2 shows the XRD patterns of the BCA(p) and BCA(aq) specimens. Comparison of the two types of biochars provides a better understanding of the effect of activation. Between 2θ (15 and 30°), one can note the presence of peaks and the absence of bumps on all samples, justifying the graphitic or non-amorphous appearance of the biochars. Non-activated biochars (BC) shows peaks above 2θ = 31° characteristic of minerals and an intense peak at 2θ = 31° attributed to silica [9]. Following activation with $ZnCl_2$ at 400°C, the peaks of the minerals Ca, Mg, and Si, which emerged above 2θ = 40° in the P400 case, disappear completely. On the other hand, the silica peak at 2θ = 31° appears only in P400(p), whose intensity has dropped by more than seven times compared with P400. A new peak appears for both activation types at 2θ = 18.2°, corresponding to $ZnCl_2$. This is due to the $ZnCl_2$ in solution, which, when converted into Zn^{2+} and Cl^- ions, becomes more reactive and is likely to react with Si. It is as if there were a cationic exchange between the minerals on the biochar surface and the Zn ions, which are eliminated by washing with acid and then distilled water [35].

Figure 2 shows that at 700°C, the intensity of the characteristic metal peaks decreases, becoming weaker in the case of P700(aq). In this figure, the $ZnCl_2$ peak disappears for P700(p) and P700(aq) and new peaks appear at 2θ (22.4 and 33.3°) and (29.8 and 36.6°) corresponding to the $Zn_2(SiO_4)$ and ZnO [36,37] peaks, respectively. The presence of the latter stems from the reaction transforming $ZnCl_2$ under the effect of temperature:

$$ZnCl_2 + H_2O \rightarrow ZnO + 2\,HCl\uparrow$$

$$2\,ZnO + SiO_2 \rightarrow Zn_2(SiO_4)$$

At higher pyrolysis temperatures (900 °C), no characteristic Zn peaks are detected. At this temperature, the reactions continue, ZnO and $Zn_2(SiO_4)$ decompose to produce gas-phase Zn capable of volatilizing according to the following reactions [38,39]. These observations indicate that the nearly complete suppression of minerals and the absence of characteristic $Zn_2(SiO_4)$ peaks in P400(aq) and P700(aq), respectively, are linked to the faster decomposition and reactivity of $ZnCl_2$ with these ions during the wet impregnation process compared to dry impregnation.

$$2\,ZnO + C \rightarrow 2\,Zn\uparrow + CO_2\uparrow$$

$$Zn_2(SiO_4) + C \rightarrow 2\,Zn\uparrow + SiO_2 + CO_2\uparrow$$

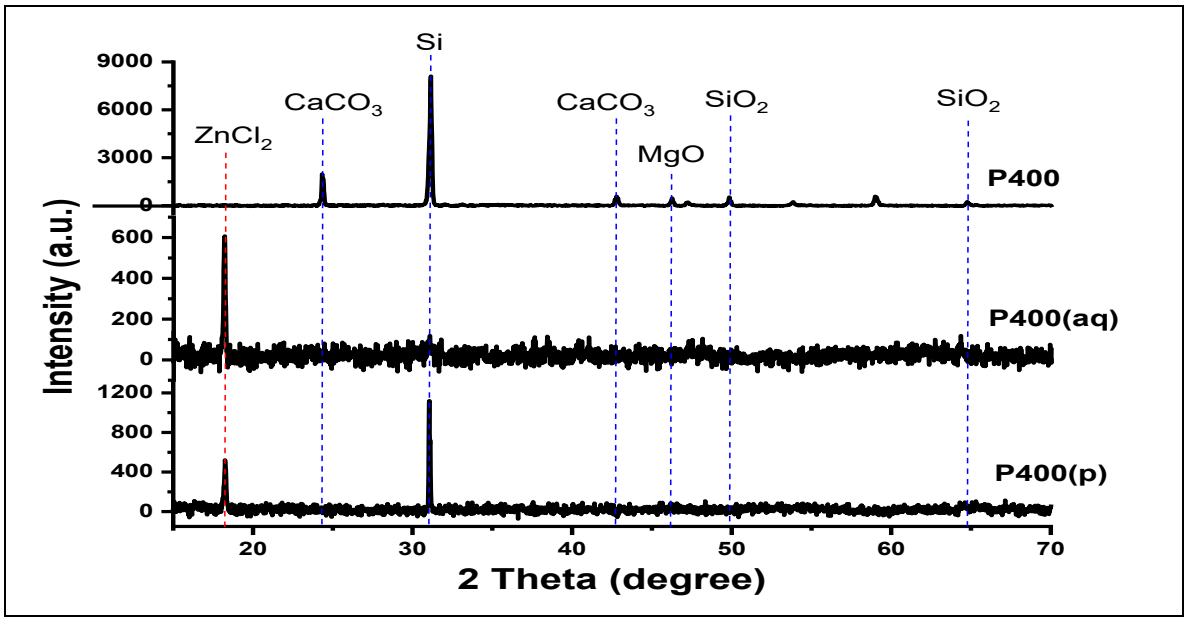

 doi:10.20944/preprints202509.2454.v1

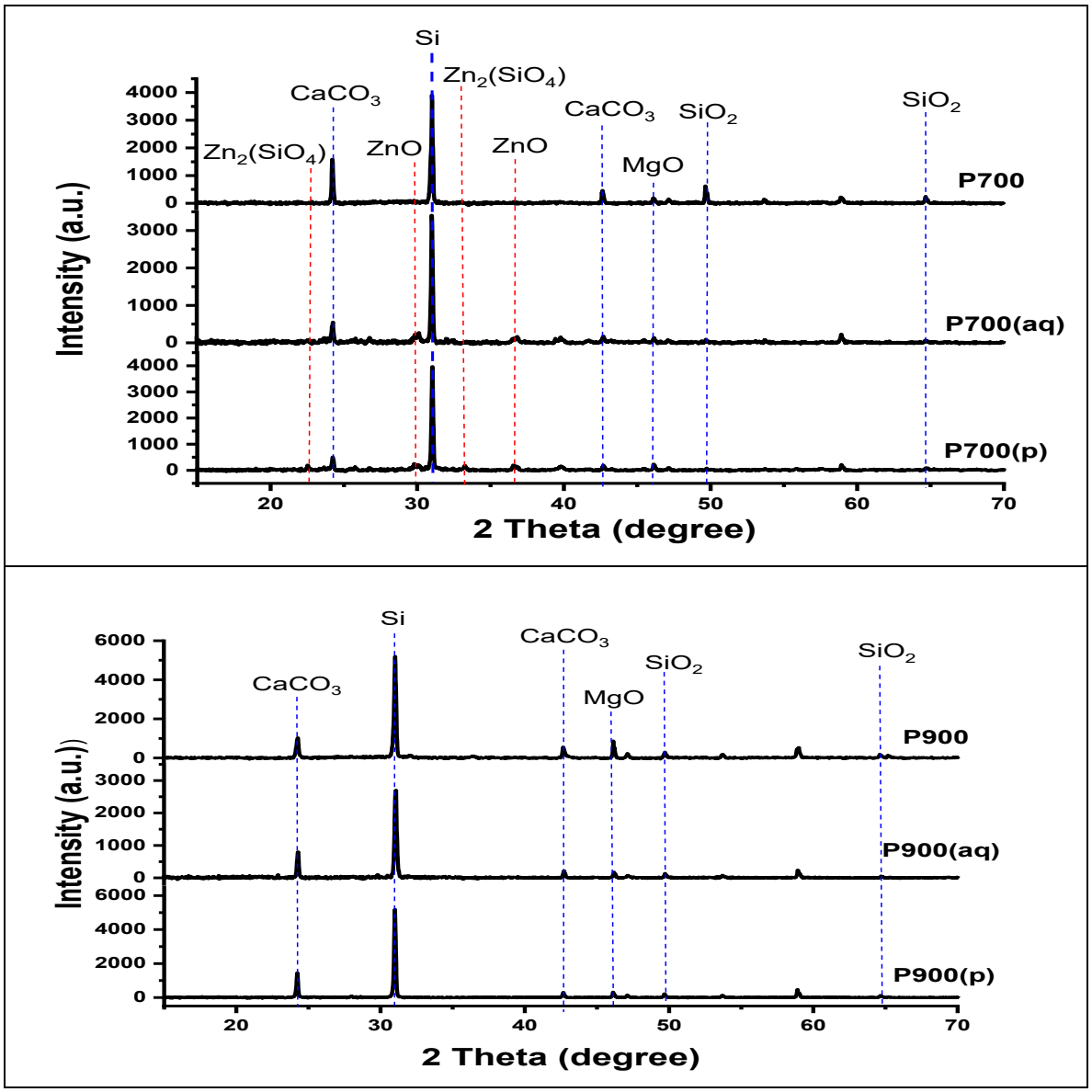

Figure 2. XRD patterns of the BCA(p), BCA(aq), and BC samples prepared by pyrolysis at 400, 700, and 900 °C.

3.3. Raman Spectroscopy

To further illustrate the structural analyses, Raman spectroscopy was performed on the prepared BCA samples, highlighting its carbon signature. Figure 3 shows the Raman spectra recorded in the 800 to 2,000 cm^{-1} energy region. In this figure, we note the presence of bands D * (1380 cm^{-1}), G (1596 cm^{-1}), S (1262 cm^{-1}), V (1506 cm^{-1}), G_L (1696 cm^{-1}), S_L (900 cm^{-1}) characteristic of sp^3 C-X (X = donor atom), graphite sp^2 C=O or sp^2 C=C, sp^3-sp^3 C-C, sp^3 C-Z (Z = heteroatom), sp^2 C=O, and sp^3 C-H, respectively [40]. Figure 4 displays a bar plot of the I_D/I_G intensity ratios for the activated biochars. Lower intensity ratios symbolize graphitization, while higher values characterize the degree of disorder in the material.

In this illustration, P400(aq) is the only material with an I_D/I_G ratio below 1, indicating a particularly ordered BCA. For other materials such as P400(p), P700(aq), P700(p), and P900(aq), P900(p), the I_D/I_G ratio remains above 1, attesting to the disordered nature of these materials [41]. These findings demonstrate that the level of disorganization gives these materials more catalytic sites and a higher adsorption capacity [42].

 doi:10.20944/preprints202509.2454.v1

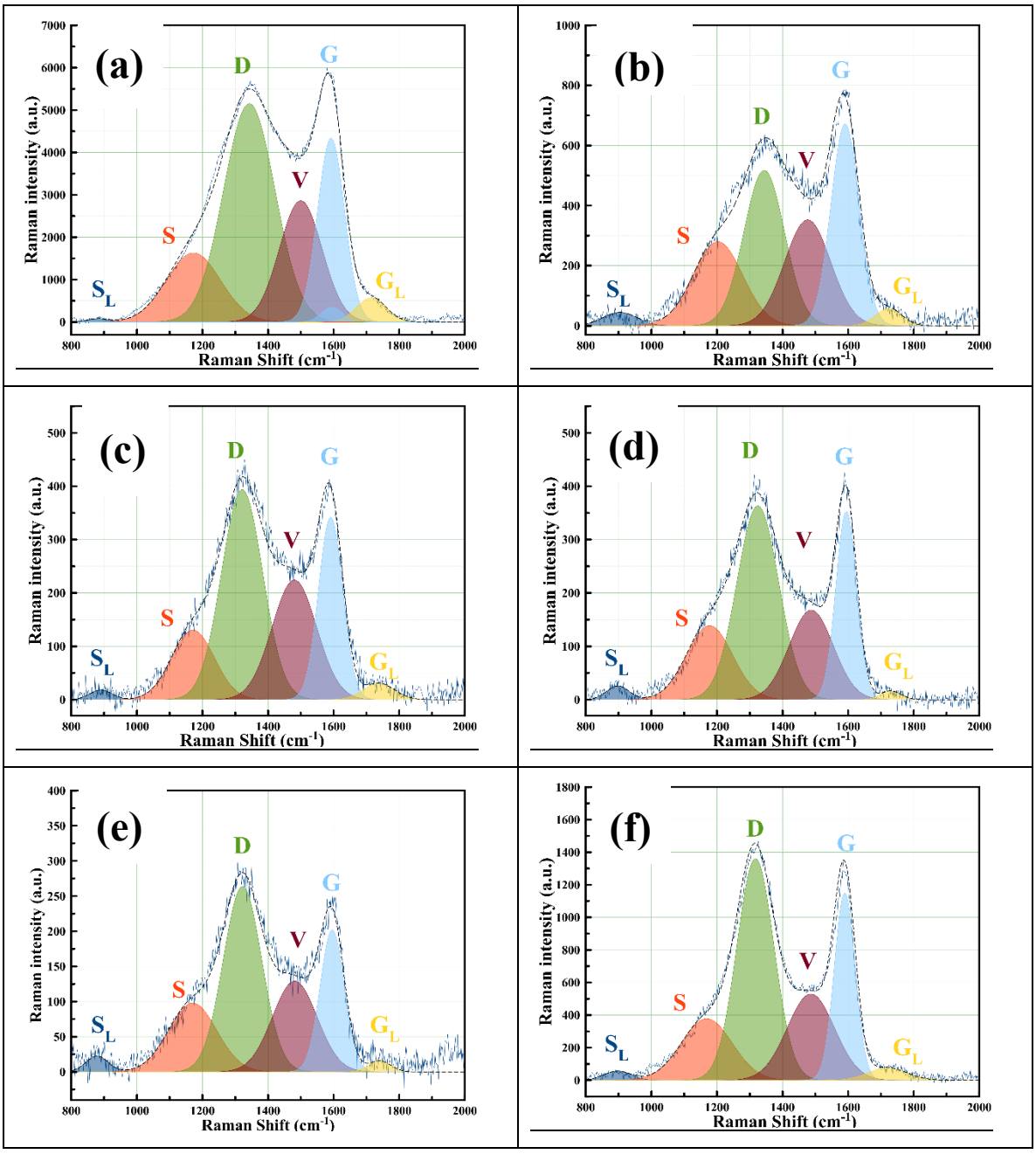

Figure 3. Raman spectroscopy of (a) P400(p), (b) P400(aq), (c) P700(p), (d) P700(aq), (e) P900(p), and (f) P900(aq).

 doi:10.20944/preprints202509.2454.v1

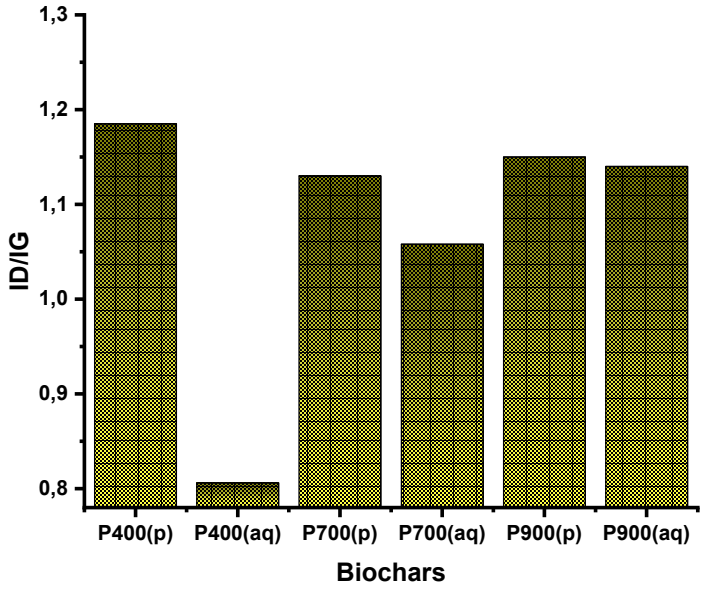

Figure 4. Bar graph of the I_D/I_G intensity ratios determined for BCAs prepared by wet and dry impregnation, at the indicated pyrolysis temperature.

3.4. XPS

Figure 5 displays XPS survey regions of activated biochar samples at the indicated pyrolysis temperature. The main peaks are Cl2p (~200 eV), C1s (~285 eV), N1s (~400 eV), O1s (~531 eV), and Zn2p (1022-1044 eV). It is worth noting the presence of zinc at the surface of P400(p), despite a thorough acid wash of the biochar, followed by rinsing with copious amounts of water. The presence of zinc, following pyrolysis at 400 °C, is due to an ionic bond between Zn(II) and chlorides, as shown by XRD. Zinc content decreases for a higher pyrolysis temperature, i.e., 700 °C, and particularly 900 °C (Figure 5). Pyrolysis at 900 °C of the dry impregnated biomass facilitates the release of zinc; its boiling temperature is 907 °C. The Zn/C atomic ratio decreases sharply with pyrolysis temperature (inset of Figure 5).

Figure 6(a,c,e) shows N1s narrow scans, fitted with either 3 or 4 components. P400(p) N1s (Figure 6a) has pyridinic (~398.5 eV), pyrrolic (~400 eV), and graphitic (401-402 eV) nitrogen atoms. It is worth noting the significant change in the shape of the N1s region, with a higher relative intensity of the pyridinic nitrogen atom component (Figure 6(c,e)), compared to the N1s peak component ascribed to pyrrolic nitrogen atoms. A fourth component can also be noted, and due to N-O (~405 eV) [43] in alkyl nitrite chemical environment [44], for activated biochar preparaed at 700 or 900 °C (Figure 6(c,e)).

Cl2p spectrum is a doublet, of which components are split by 1.6-1.7 eV, with an intensity ratio $Cl2p_{3/2}/Cl2p_{1/2}$= 2. The doublet peak position is in line with the C-Cl bond for the biochar prepared at 400 °C (Figure 6b). For pyrolysis conducted at 700 and 900 °C, a second doublet is noted and assigned to chlorides (Figure 6(d,f)). The presence of Cl^- could be due to remaining $ZnCl_2$, C-Cl bond cleavage, and retention of the chlorides, despite thorough rinsing with water. Another possible reason for the presence of chlorides is the reaction of biochar-Cl with ZnO at moderate temperature, which induces the reduction of Zn(II) into zero valent zinc, hence the appearance of chlorides [45]. The concomitant presence of Cl^- and N-O bonds on the biochar surface for high pyrolysis temperature is likely to be related to the disorder in the biochar structure, observed in the Raman spectra of P700(p) and P900(p).

 doi:10.20944/preprints202509.2454.v1

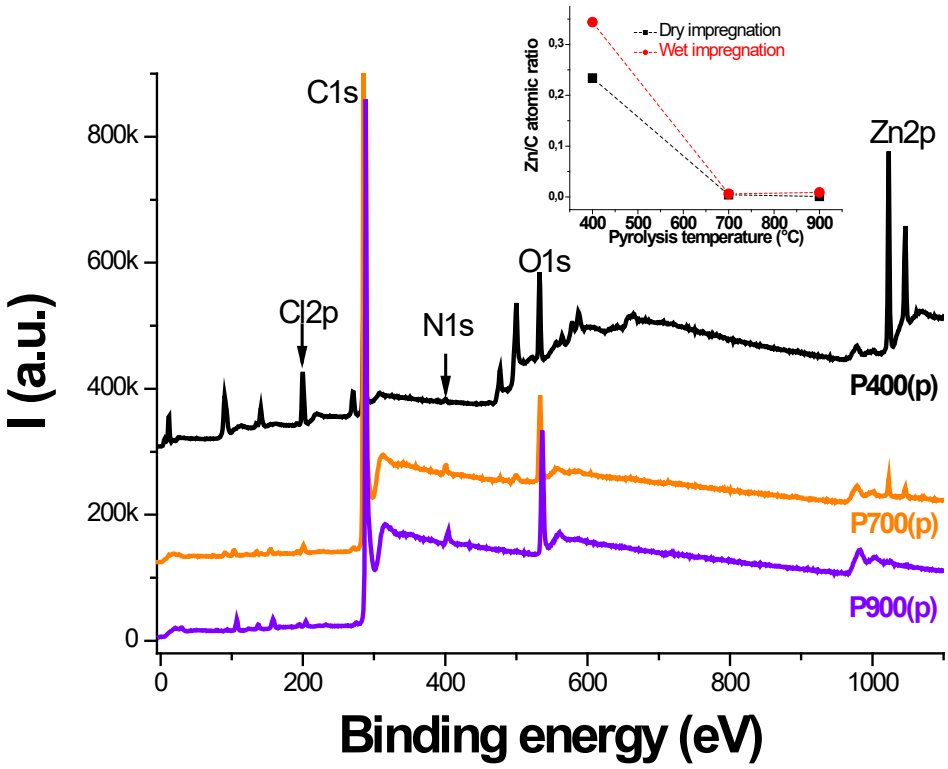

Figure 5. Survey spectra of activated biochar prepared by pyrolysis at 400, 700, and 900 °C. Zn/C atomic ratio-vs-temperature is shown in the inset.

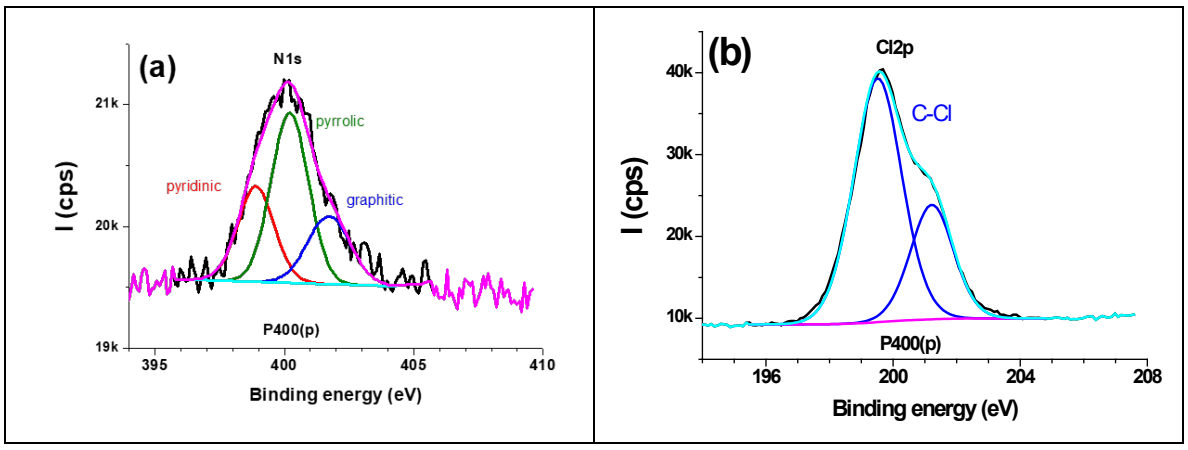

 doi:10.20944/preprints202509.2454.v1

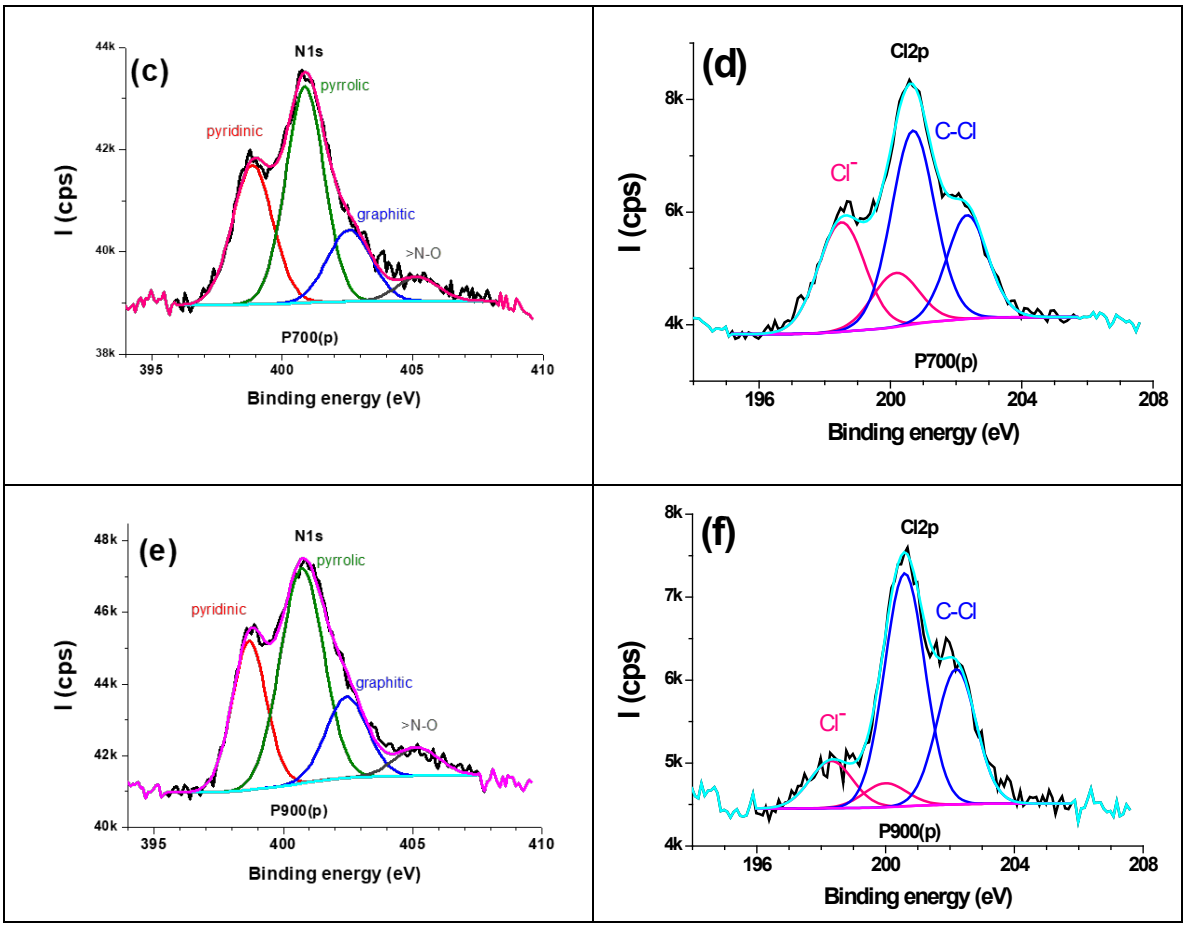

Figure 6. High-resolution, peak-fitted N1s and Cl2p spectra of (a,b) P400(p), (c,d) P700(p), and (e,f) P900(p).

3.5. Determination of MB and Iodine Indices

The histogram of methylene blue index and iodine index values for the various active biochars is shown in Figure 7. Figure 7a shows, for dry impregnation, that the N_I of BCA(p) increases from P400(p) to P700(p), with N_I values of 274 and 664 mg.g^{-1}, respectively, then decreases to 473.3 mg.g^{-1} for P900(p). For BCA(aq), there is a gradual increase in N_I value as a function of pyrolysis temperature. The results show that P700(p) has the highest N_I value, demonstrating that microporosity is affected by both temperature and activation type. As shown in Figure 7b, N_{MB} values increase with pyrolysis temperature, reaching near their maximum at 700 °C for the BCA(p) and BCA(aq) cases. This figure indicates that for P400(p) and P400(aq), N_{MB} values remain low, below 40 mg.g^{-1}. This trend suggests that mesoporosity depends on temperature and volatile substance concentration.

 doi:10.20944/preprints202509.2454.v1

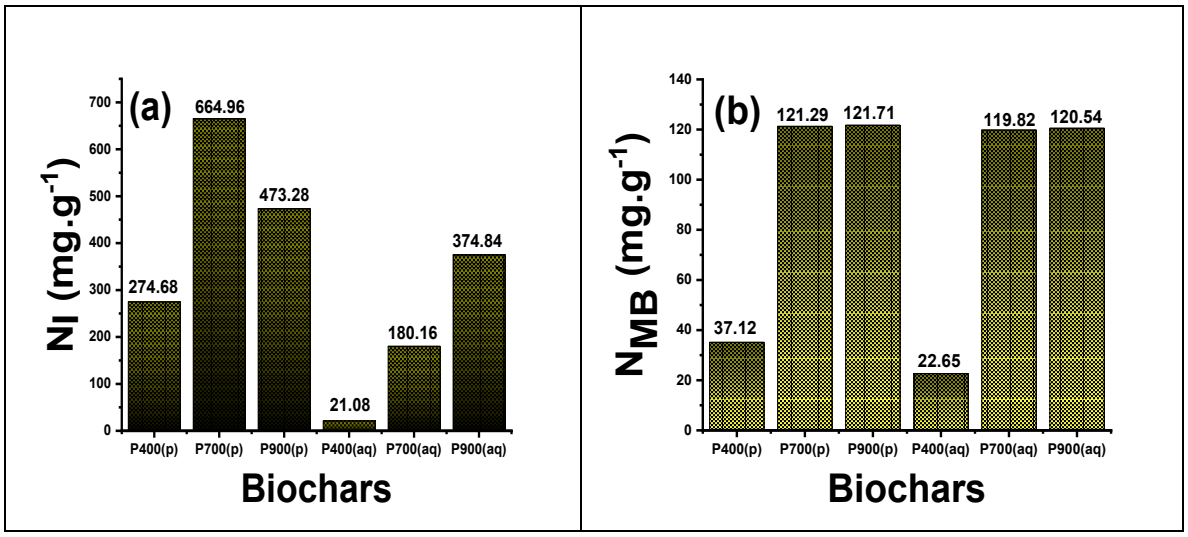

Figure 7. Iodine number (a), and methylene blue number (b) of BCAs.

3.6. Electrochemical Characterization

Figure 8 illustrates the study of the electrochemical properties of the surface of GC electrodes modified with different BCA materials, such as P400(aq), P400(p), P700(p), P700(aq), P900(p), and P900(aq) was carried out by cyclic voltammetry and impedance spectroscopy. These cyclic voltamograms all display the same quasi-rectangular symmetrical arrangement with no oxidation or reduction points (peaks). This result suggests an EDC energy storage behavior of these composite biochar materials [46], which is consistent with porous carbon-based materials [47]. Furthermore, a comparative study of the CV profile of the different biochar materials P400(aq), P400(p), P700(p), P700(aq), P900(p), and P900(aq) reveals a significantly higher overall surface area for P700(p), indicating that this material has better electroactivity. In other words, pyrolysis at 700 °C gives biochars superior conductivity compared to others, attesting to their outstanding performance and ideal capacitance characteristics. Electrochemical impedance spectroscopy (EIS) measurements were also carried out for BCA coatings deposited on GC to assess the interracial properties of GC electrodes, specifically P400(aq), P400(p), P700(aq), P700(p), P900(aq), and P900(p). Figure 8b shows the Nyquist curves obtained at open circuit potential in 0.5 M H_2SO_4. As observed, the Nyquist curves consist of a semicircle appearing in the high-frequency region and a slope in the low-frequency region, reflecting ideal supercapacitive behavior [48]. A study of the electron transfer capacities of the various electrodes showed that the presence of BCA on the surface of the GC electrode induces a significant decrease in charge transfer resistance (Rct), leading to the conclusion that the bran millet matrix is sufficiently conductive. Rct values decrease in the following order: GCE (168 Ω) > P400(aq) (144 Ω) > P400(p) (50.3 Ω) > P700(aq) (40.4 Ω) > P900(aq) (19.1 Ω) > P900(p) (18.3 Ω) > P700(p) (2.5 Ω). The lower charge transfer resistance value of the P700(p) electrode material indicates an easier electron transfer process, obtained for dry impregnation and pyrolysis at 700 °C. These results indicate that the obstructive effect of pores leads to a reduction in the rate of electron transfer or an increase in resistance to electron flow [49]. Figure 9 (a, b, c) summarizes a correlation determined between the indices and the specific capacity as well as the geometric mean of the N indices ($\tilde{n} = \sqrt{N_I \times N_{MB}}$). It is observed that BCA(p) displays higher indices, Csp, and geometric means compared to BCA(aq). These results could be attributed to the release of $ZnCl_2$-occupied pores. Csp values increase in relation to indices (N_I or N_{MB}) and pyrrolysis temperature for BCA(aq). For BCA(p), this progression reaches its maximum at P700(p). A similar trend is observed for the Csp curve in relation to the geometric mean, an indication that the specific capacity of a material is highly dependent on its microporosity [50], which provides a larger active surface area and facilitates the accumulation of a large number of surface ions [51]. The presence of mesopores can increase the specific capacity by adsorbing electrolyte ions larger than the diameters of the micropores [23]. The combination of

 doi:10.20944/preprints202509.2454.v1

micropores and mesopores in a material would be a great asset to consider. The electrochemical and spectroscopic characterizations all show that the P700(p) material has optimal characteristics, so it will be chosen in the remainder of this work as the electrode material for studying the supercapacitive properties of BCAs in galvanostatic measurements. Biochars produced by the dry impregnation method have a higher activity than those produced by wet impregnation. This is due to the fact that the activating agent $ZnCl_2$ and the material decompose simultaneously and interact more readily in dry impregnation, enabling full pore release and offering these materials improved performance. It is important to note that $ZnCl_2$ melts at about 290 °C, and the forming biochar is dispersed in pure $ZnCl_2$ liquid, which is probably more efficient than in the case of wet impregnation where $ZnCl_2$ is much more dispersed.

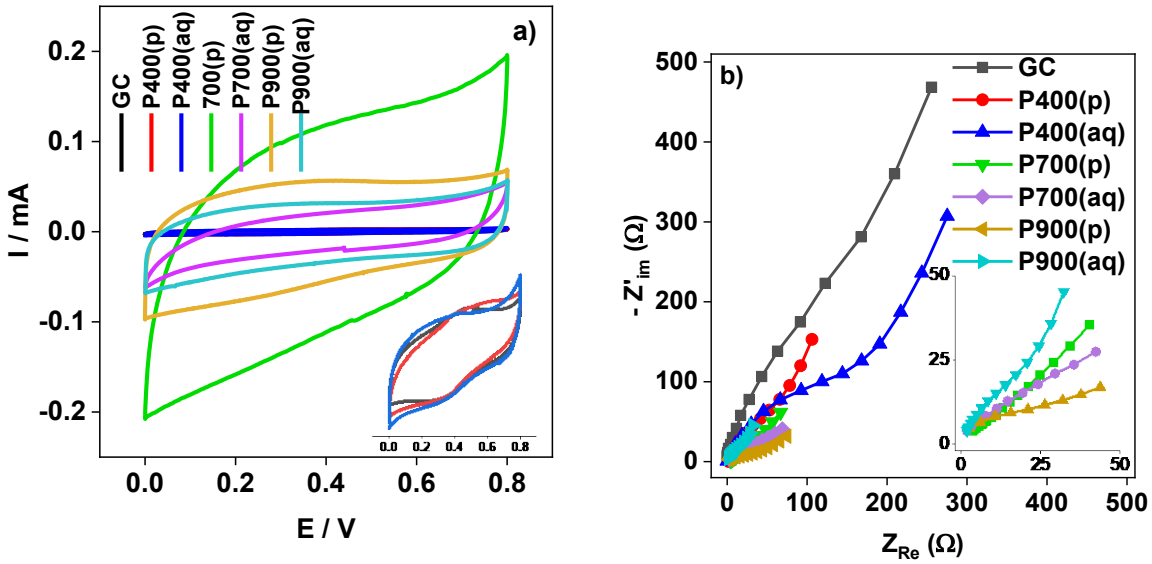

Figure 8. (a) CV curves, and (b) EIS plots recorded for GC and activated biochar electrode materials.

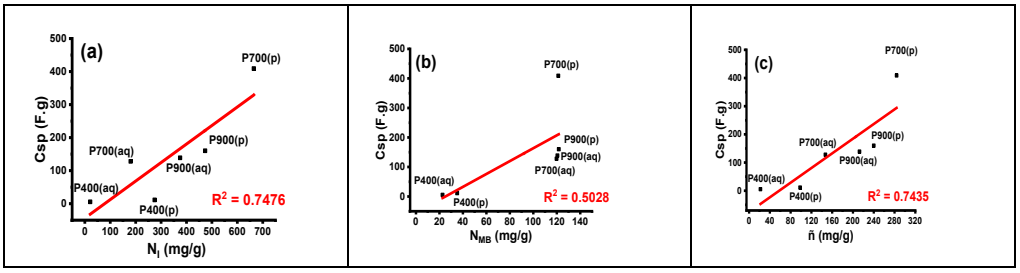

Figure 9. Plots of specific capacitance (Csp) versus (a) iodine number, (b) methylene blue number, and (c) the geometric mean value of N_{MB} and N_I.

3.7. Supercapacitor Studies

The supercapacitive behavior of the P700(p) electrode material was assessed in a 0.5 M H_2SO_4 electrolyte solution using the three-electrode setup described above. The CV and Csp curves, as a function of sweep rate variation (10 to 100 mV/s), are shown in Figure 10 (a and b, respectively). The area of the cyclic voltammograms increases with scan speed without any distortion, indicating efficient ion transport and excellent capacitive behavior of the P700(p) material [52]. Additionally, the shape of the voltammograms suggests the presence of an EDLC. Regarding Csp, it decreases with scan rate, from 673 $F.g^{-1}$ at 10 mV/s to 341 $F.g^{-1}$ at 100 mV/s. This trend is because, at lower scan speeds, ions in the electrolyte have less kinetic energy, allowing more time for migration and diffusion into the BCA micropores [53]. The GCD curves obtained at different current densities ranging from 0.5 to 5 $A.g^{-1}$ (Figure 10c) shows a decrease in charge/discharge times as the applied current increases. Both low sweep rates and low current densities promote maximum charge storage across the active sites.

 doi:10.20944/preprints202509.2454.v1

Unlike the cyclic voltammograms, the GCD curves do not show perfect potential-time linearity, likely due to the internal resistance of the material or difficulty in accessing small pores [42].

From GCD measurements (Figure 10c), a specific capacitance of 440 $F.g^{-1}$ was obtained at a current density of 0. 5 $A.g^{-1}$, and ~175 440 $F.g^{-1}$ for a current density of 5 $A.g^{-1}$ (Figure 10f). The cyclic stability test, which assesses the electrochemical stability of electrode materials over multiple cycles, was performed on BCA P700(p) at a scan speed of 50 mV/s for 5000 cycles. The CV, Csp, and retention capacity curves as a function of cycle number are shown in Figure 10 (d and e). It is evident that this novel biochar material, derived from millet bran, exhibits good stability, with a retention capacity of ~130 %, after 5000 cycles. The significant increase in capacitive retention is likely caused by continuous electrochemical activation [54] of inaccessible catalytic sites, thereby improving electron transfer at the electrode/electrolyte interface. In other words, certain sites become activated as the number of cycles increases, which in turn boosts the retention capacity during cycling [23,55]. These results show a remarkable retention capacity for the P700(p) electrode material and are in line with other studies. Zhu et al. [55] reported an increase of capacitive retention as high as 242.9% after 10,000 cycles for N-doped Cu_7S_4/carbon felt, whereas Wang et al. [56] reported a capacitive retention of 120% after 5000 cycles for CO_3O_4@MnO_2@PPy/activated carbon. The group of Maboudian [54] reported an increase of 150% in the capacitive retention for unactivated carbon, in H_2SO_4, which is in line with the results discussed in this work. A polyaniline/carbon composite was found to be highly stable with a capacitive retention of 225% after 10,000 cycles [57]. Figure 10f displays a plot of specific capacitance versus the current density.

Table 1 illustrates the specific capacitance values of various electrode materials cited in the literature, developed from metal oxide and biochar. P700(p) exhibits a Csp that exceeds those of modified metal oxides and some biochars. However, it has lower capacity values than BC@MnO_2 which is based on MnO_2, a well-known supercapacitor, whereas SGB has a higher specific capacitance but the capacitive retention levels off at 107% after 12,000 cycles. Nevertheless, the millet bran-derived biochar is an excellent energy storage material that meets the requirements of green, renewable energy. For P700(p), an energy density (E) of 39.1 Wh. kg^{-1} and a power (P) of 0.20 $kW.kg^{-1}$ were determined. This material demonstrates excellent electrochemical properties, meeting the requirements for supercapacitors and batteries, which are often limited by their energy density values, typically below 20.0 Wh. kg^{-1} [58]. Interestingly, it is obatianed at moderate pyrolysis temperature and without the use of an excessive initial $ZnCl_2$/biomass ratio.

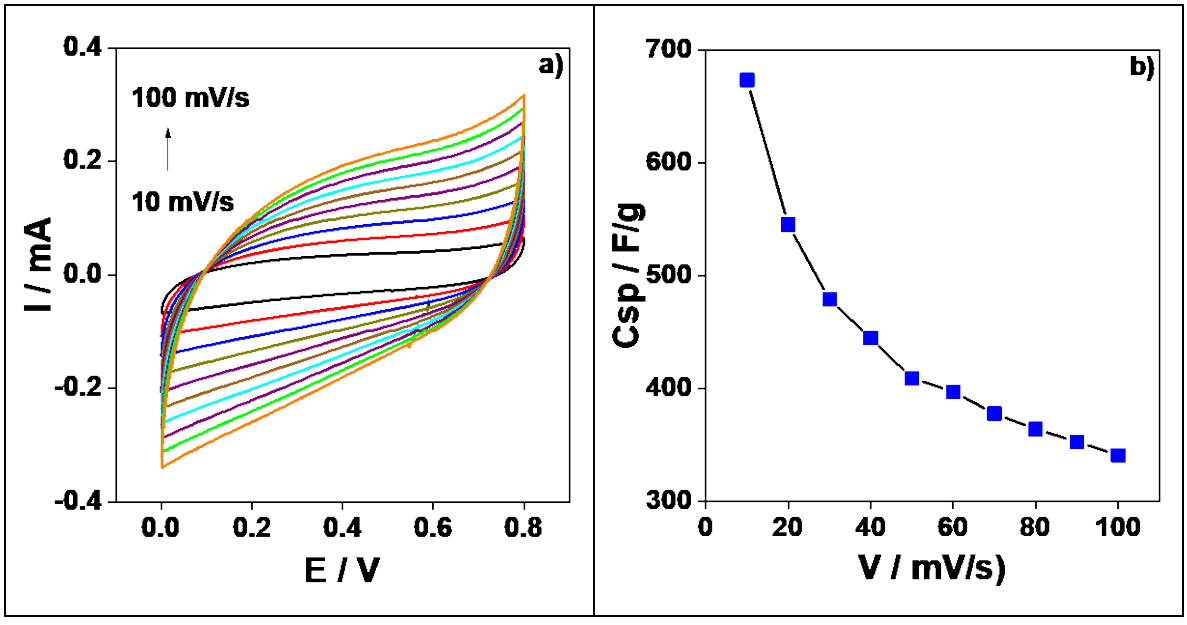

 doi:10.20944/preprints202509.2454.v1

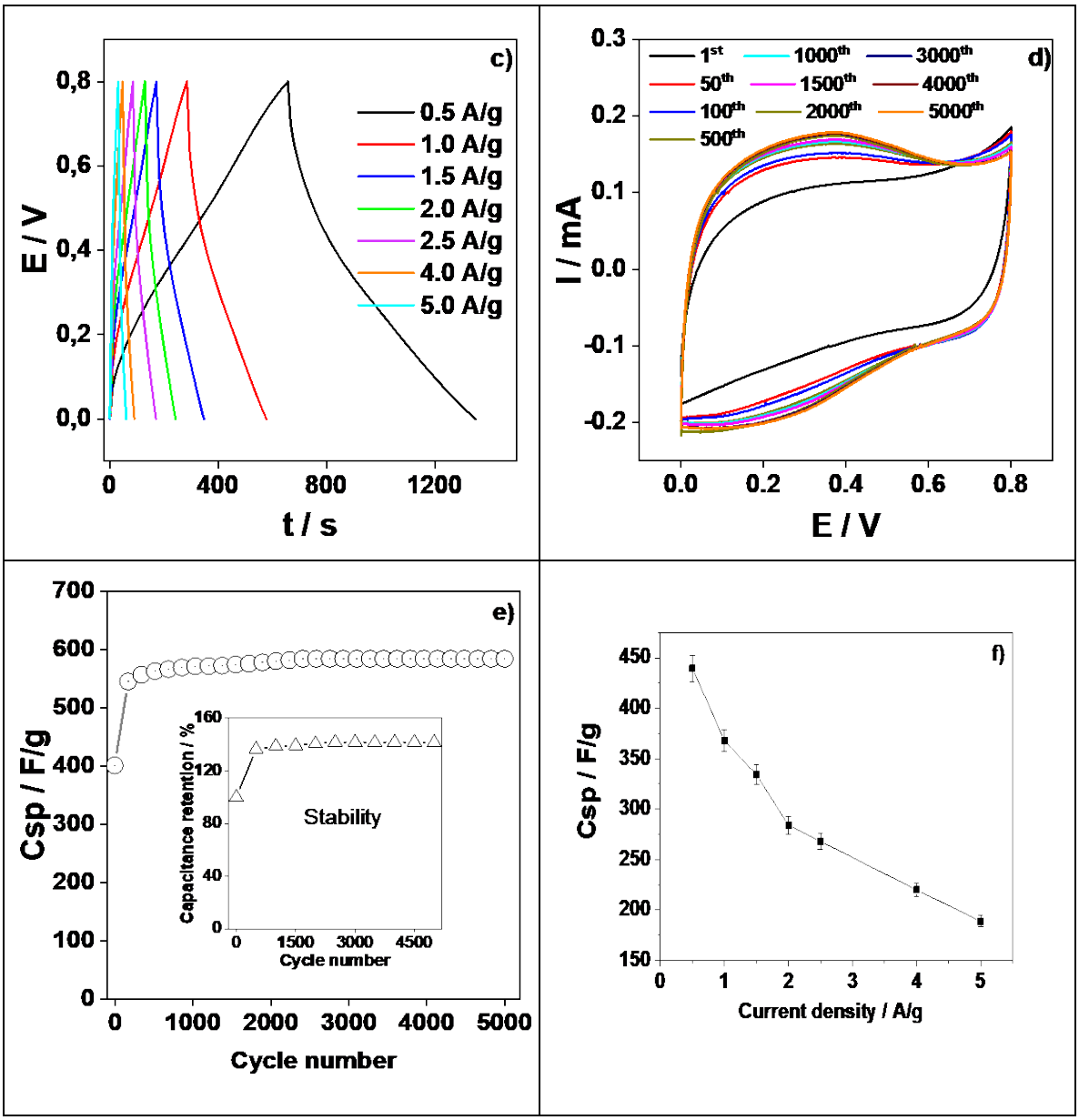

Figure 10. (a) CV and (b) Csp curves versus scan rate variation (10 to 100 mV/s), (c) GCD curves at different current densities, (d) CV and (e) Csp and retention capacity curves versus cycle number, and (f) specific capacitance versus the current density plot.

Table 1. Comparison of Csp values of P700(p) and those of related materials.

Electrode materiels	Electrolyte	Current density (A/g)	Csp (F/g)	Ref
Fe_2O_3/GA	0.5 M Na_2SO_4	1	81.3	[59]
NCA	1 M H_2SO_4	0.1	NCA-800: 166 NCA-900: 136	[60]
HC2	2 M KOH	0.5	80	[61]
Biochar litchi seed	1 M H_2SO_4	1	190	[62]
Biochar apricot shell	3 M KOH	0.5	216	[63]
BC@MnO_2	1 M Na_2SO_4	0.5	512	[64]
SGB-700	1 M H_2SO_4	0.5	638	[65]
RSBC	6 M KOH	0.2	RSBC: 197.2 RSBC-2: 296	[66]
P700(p)	0.5 M H_2SO_4	0.5	440	This work

 doi:10.20944/preprints202509.2454.v1

Fe2O3/GA: nano-iron oxide (Fe2O3)/three-dimensional graphene aerogel. **NCA**: nitrogen-doped carbon aerogels. **Biochar litchi seed**: Litchi seed-derived biochar. **Biochar apricot shell**: apricot shell-derived biochar activated by KOH. **BC@MnO2**: Acacia leucopheloea wood sawdust (ALWSD) biochar-supported MnO_2 nanocomposite. **SGB-700**: Suaeda Glauca Bunge (SGB) derived biochar. **RSBC:** rice straw biochar activated at 800 °C. **RSBC-2:** rice straw biochar activated at 800 °C with KOH. **HC2:** nitrogen-doped hydrochar from sawdust biomass actived with KOH.

Conclusion

Activated biochars were prepared by impregnation of millet bran biomass with $ZnCl_2$ powder or $ZnCl_2$ solution (dry and wet impregnation). Both the temperature and the way the biomass was activated affected the electrochemical performance of the biochars. Porosity was monitored via iodine and methylene blue indices. XPS analysis showed the absence of zinc at high pyrolysis temperature, and suggested complex reaction between $ZnCl_2$ and the biochar leading to C-Cl bonds, and also tightly bound zinc at low pyrolysis temperature, despite post acid wash of the biochar. These observations were corroborated by XRD, which confirmed the absence of zinc-specific peaks after acid washing, particularly in the case of P700(p). SEM pictures of BCAs revealed well elaborated pores, helping to increase electron transport and improve material conductivity. Electrochemical analyses have demonstrated the superior energy storage performance of an EDLC supercapacitor at optimum efficiency. The P700(p) material had the highest N_I value, a significant N_{MB} value, and a specific capacitance of 440 $F.g^{-1}$ at 0.5 A/g, with an energy density of 39.1 W h kg^{-1}. Moreover, the capacitive retention is 130% after 5000 cycles, possibly due to electrochemical activation during the charge-discharge process. This work demonstrates that the $ZnCl_2$ activating agent used in the dry impregnation method confers exceptional electrochemical performance on the materials. These results highlight the opportunity to exploit materials derived from bio-waste for energy storage systems, which not only helps to address environmental issues but also optimizes the economic and performance metrics of supercapacitors, thus contributing to addressing UNs' SDG7 relevant to Affordable and Clean Energy.

CRediT Authorship Contribution Statement: Cheikh Ahmadou Bamba Diop: Writing – review & editing, Writing –original draft, Validation, Conceptualization, Data Curation. **Déthié Faye**: Writing – review & editing, Writing – original draft, Validation. **Momath Lo**: Writing–review & editing, Writing – original draft, Validation, Conceptualization. **Dahbia Bakiri**: Investigation, Formal analysis, Writing-review & editing. **Huifeng Wang**: Visualization, Validation, Investigation. **Mohamed El Garah**, Investigation, Data Curation, Writing–review & editing, **Vaishali Sharma**: Investigation, Data Curation, Writing–review & editing, **Aman Mahajan**: Investigation, Validation, Writing–review & editing, **Mohamed Jouini**: Investigation, Validation, Writing–review & editing. **Diariatou Gningue-Sall**: Funding, Conceptualization, Writing–review & editing. **M. Chehimi**: Conceptualization, Data curation, Validation, Writing – review & editing, Supervision.

Data Availability: Data will be made available on request

Declaration of Competing Interest: The authors declare that they have no known competing financial interests or personal relationships that could have appeared to influence the work reported in this paper.

References

1. S. Jellali, P. Dutournié, M. Jeguirim, Materials and clean processes for sustainable energy and environmental applications: Foreword, 26, 3-5, (2023).
2. A. A. Kebede, T. Kalogiannis, J. V. Mierlo, M. Berecibar, A comprehensive review of stationary energy storage devices for large scale renewable energy sources grid integration, Renewable Sustainable Energy Rev., 159, 112213, (2022).
3. M. E. Şahin, Frede Blaabjerg, A. Sangwongwanich, A Comprehensive Review on Supercapacitor Applications and Developments, Energies, 15, 674, (2022).

 doi:10.20944/preprints202509.2454.v1

4. S. Sharma, P. Chand, Supercapacitor and electrochemical techniques: A brief review, Results Chem., 5, 100885, (2023).
5. M. A. Dar, S. R. Majid, M. Satgunam, C. Siva, S. Ansari, P. Arularasan, S. R. Ahamed, Advancements in Supercapacitor electrodes and perspectives for future energy storage technologies, I. J. Hydrogen Energy, 70, 10-28, (2024).
6. Z. Zhai, L. Zhang, T. Du, B. Ren, Y. Xu, S. Wang, J. Miao, Z. Liu, A review of carbon materials for supercapacitors, Mater. Des, 221, 111017, (2022).
7. W. Chen, X. Shi, Y. Peng, Y. Wang, J. Li, Y. Wang, C. Gong, C. Dong, S. Gao, L. Xu, Z. Fang, H. Yang, Biomass pyrolysis for N-doped biochar: Relationship among preparation process, N-doped biochar properties, and supercapacitors, Fuel, 404, 136372, (2026).
8. F. Mahmood, M. Ali, M. Khan, C. F. M. Mbeugang, Y. M. Isa, A. Kozlov, M. Penzik, X. Xie, H. Yang, S. Zhang, B. Li, A review of biochar production and its employment in synthesizing carbon-based materials for supercapacitors, Ind. Crops Prod., 227, 120830, (2025).
9. C. A. B. Diop, M. Lo, Y. Snoussi, S. Gam-Derouich, M. E. Garah, M. Jouini, D. Gningue-Sall, M. M. Chehimi, Functional hydrochar/biochar through thermochemical conversion of millet Bran from Senegal: physicochemical, morphological and electrochemical properties, emergent mater., 8, 2663–2678, (2025).
10. M. Ahmad, A. U. Rajapaksha, J. E. Lim, M. Zhang, N. Bolan, D. Mohan, M. Vithanage, S. S. Lee and Y. S. Ok, « Biochar as a sorbent for contaminant management in soil and water: A review », Chemosphere vol. 99, pp. 19–33, (2014).
11. D. Wang, C. Li, S. J. Parikh and K. M. Scow, «Impact of biochar on water retention of two agricultural soils – A multi-scale analysis», Geoderma, vol. 340, pp.185-191, (2019).
12. A. Kumar, K. Sharma and A. R. Dixit, «Carbon nanotube- and graphene-reinforced multiphase polymeric composites: review on their properties and applications», J. Mater., vol. 55, pp. 2682-2724, (2020).
13. M. Bassyouni, A. E. Mansi, A. Elgabry, B. A. Ibrahim, O. A. Kassem and R. Alhebeshy, Utilization of carbon nanotubes in removal of heavy metals from wastewater: a review of the CNTs' potential and current challenges, Appl. Phys. A: Mater. Sci. Process. Vol. 126, pp. 1-33, (2020).
14. X. Li, J. Zhang, B. Liu, Z. Su, A critical review on the application and recent developments of post-modified biochar in supercapacitors, J. Cleaner Prod., 310, 127428, (2021).
15. Uppugalla, S., Pothu, R., Boddula, R. et al. Nitrogen and sulfur co-doped activated carbon nanosheets for high-performance coin cell supercapacitor device with outstanding cycle stability. emergent mater. 6, 1167–1176 (2023). https://doi.org/10.1007/s42247-023-00503-1
16. Sandeep, A., Ravindra, A.V. Peanut shell-derived porous carbons activated with iron and zinc chlorides as electrode materials with improved electrochemical performance for supercapacitors. emergent mater. 8, 235–250 (2025). https://doi.org/10.1007/s42247-024-00935-3
17. Gęca, M., Khalil, A. M., Tang, M., Bhakta, A. K., Snoussi, Y., Nowicki, P., Wiśniewska, M., Chehimi, M. M. (2023). Surface treatment of biochar—methods, surface analysis and potential applications: a comprehensive review. Surfaces, 6(2), 179-213.
18. N. Hagemann, K. Spokas, H.-P. Schmidt, R. Kägi, M. A. Böhler and T. D. Bucheli, Activated Carbon, Biochar and Charcoal: Linkages and Synergies across Pyrogenic Carbon's ABCs, vol. 182, pp. 1-19, (2018).
19. K. Velusamy, J. B. Isabel, S. Periyasamy, A. Thiruvenkadam, H. Ravikumar, S. K. Gupta, E. A. Lopez-Maldonado, Role of biochar as a greener catalyst in biofuel production: Production, activation, and potential utilization – A review, J. Taiwan Inst. Chem. Eng., 1-18, 105732, (2024).
20. X. Yuan, Y. Cao, J. Li, A. K. Patel, C.-D. Dong, X. Jin, C. Gu, A. C.K. Yip, D. C.W. Tsang, Y. S. Ok, Recent advancements and challenges in emerging applications of biochar-based catalysts, Biotechnol. Adv., 67, 108181, (2023).
21. X. Zhou, Y. Zhu, Q. Niu, G. Zeng, C. Lai, S. Liu, D. Huang, L. Qin, X. Liu, B. Li, H. Yi, Y. Fu, L. Li, M. Zhang, C. Zhou, J. Liu, New notion of biochar: A review on the mechanism of biochar applications in advannced oxidation processes, Chem. Eng. J. 416, 129027, (2021).
22. H. I. Abdu, S. Adnan, T. Aboudou, Y. Guo, L. N. nian, L. Xiaowei, L. Ziyu, K. Eid, Hierarchical porous carbon biochar nanotubes encapsulated metal nanocrystals with a strong metal-carbon interaction for high-performance supercapacitors, Ultrason. Sonochem., 107476, (2025).

 doi:10.20944/preprints202509.2454.v1

23. R. M. A. P. Lima, G. S. dos Reis, M. Thyrel, J. J. Alcaraz-Espinoza, S. H. Larsson, H. P. de Oliveira, Facile Synthesis of Sustainable Biomass-Derived Porous Biochars as Promising Electrode Materials for High-Performance Supercapacitor Applications. *Nanomaterials 12*, 866, (2022).
24. J. Sun, L. E, C. Ma, S. Luo, Z. Wu, W. Li, S. Liu, Effects of the Pore Structure of Commercial Activated Carbon on the Electrochemical Performance of Supercapacitors, K. Zhang, J. Energy Storage, 45, 103457, (2022).
25. T. Jamnongkan, N. Intaramongkol, N. Kanjanaphong, K. Ponjaroen, W. Sriwiset, R. Mongkholrattanasit, P. Wongwachirakorn, K.-Y. A. Lin, C.-F. Huang, Study of the Enhancements of Porous Structures of Activated Carbons Produced from Durian Husk Wastes, Sustainability, 14, 5896, (2022).
26. Porosity Analysis of Acacia catechu Seed-derived Carbon Materials Activated with Sodium Hydroxide and Potassium Hydroxide: Insights from Methylene Blue and Iodine Number Methods, P. K. Mishra, S. Aryal, H. B. Oli, T. Shrestha, D. Jha, R. L. (Swagat) Shrestha, D. Pr. Bhattarai, J. Nepal Chem. Soc., 45, 57-65, (2025).
27. C. A. Nunes, M. C. Guerreiro, Estimation of surface area and pore volume of activated carbons by methylene blue and iodine numbers, Quim. Nova, 34, 3, 472-476, (2011).
28. C. Du, B. Liu, J. Hu, H. Li, Determination of iodine number of activated carbon by the method of ultraviolet–visible spectroscopy. Mater. Lett., 285, 129137, (2021).
29. M. Lo, M. Tang, D. Faye, V. Vaiyapuri, A. Jayaram, N. Mani, M. Jouini, M. M. Chehimi, Silver-modified sugarcane bagasse biochar-based electrode materials for the electrochemical detection of mercury ions in aqueous media, Electrochimica Acta, 540, 147214, (2025).
30. S. Umino and J. Newman, Diffusion of sulfuric acid in concentrated solutions, J. Electrochem. Soc. 140, 2217-2221, (1993).
31. D. Faye, M. Lo, D. Seye, C.A.B. Diop, M.G. Diop, A. Ngom, M. Dieng, A.K. Bhakta, D.G. Sall, M.M. Chehimi, A. Koné, Silver Nanoparticles Supported by Carbon Nanotubes Functionalized with 1, 2, 3-Benzenetricarboxylic Acid: Spectroscopic Analysis and Electrochemical Capacitance, J. Inorg Organomet Polym Mater. 1-14 (2025).
32. D. Thomas, N. B. Fernandez, M. D. Mullassery and R. Surya, Iron oxide loaded biochar/polyaniline nanocomposite: Synthesis, characterization and electrochemical analysis, Inorg. Chem. Com., 119, 1-10, (2020).
33. B. Li, C. Li, D. Li, L. Zhang, S Zhang, Z. Cui, D. Wang, Y. Tang, X. Hu, Activation of pine needles with zinc chloride: Evolution of functionalities and structures of activated carbon versus increasing temperature, Fuel Process. Technol., 252, 107987, (2023).
34. L. Yan, Y. Liu, Y. Zhang, S. Liu, C. Wang, W. Chen, C. Liu, Z. Chen, Y. Zhang, $ZnCl_2$ modified biochar derived from aerobic granular sludge for developed microporosity and enhanced adsorption to tetracycline, Bioresource Technology, 297, 122381, (2020).
35. J. Zhao, D. Zhou, J. Zhang, F. Li, G. Chu, M. Wu, B. Pan, C. E.W. Steinber, The contrasting role of minerals in biochars in bisphenol A and sulfamethoxazole sorption, J. Pre-proof, 264, 128490, (2021).
36. D. Xia, F. Tan, C. Zhang, X. Jiang, Z. Chen, H. Li, Y. Zheng, Q. Li, Y. Wanga, $ZnCl_2$-activated biochar from biogas residue facilitates aqueous As(III) removal, Appl. Surf. Sci., 377, 361-369, (2016).
37. A. S. Yusuff, M. A. Lala, K. A. Thompson-Yusuff, E. O. Babatunde, $ZnCl_2$-modified eucalyptus bark biochar as adsorbent: preparation, characterization and its application in adsorption of Cr(VI) from aqueous solutions, South Afr. J. Chem. Eng., 42, 138–145, (2022).
38. S. Minaei, K. Z. Benis, K. N. McPhedran, J. Soltan, Evaluation of a $ZnCl_2$-modified biochar derived from activated sludge biomass for adsorption of sulfamethoxazole, Chem. Eng. Res. Des., 190, 407–420, (2023).
39. S. Wei, Q. Qin, Z. Liu, Thermal behavior analysis and reaction mechanism in the preparation of activated carbon by $ZnCl_2$ activation of bamboo fibers, J. Anal. Appl. Pyrolysis, 179, 106500, (2024).
40. M. W. Smith, I. Dallmeyer, T. J. Johnson, C. S. Brauer, J.-S. McEwen, J. F. Espinal, M. Garcia-Perez, Structural analysis of char by Raman spectroscopy: Improving band assignments through computational calculations from first principles, Carbon, 100, 678-692, (2016).
41. M. Ayiania, E. Weiss-Hortala, M. Smith, J.-S. McEwen and M. Garcia-Perez, Microstructural analysis of nitrogen-doped char by Raman spectroscopy: Raman shift analysis from first principles, Carbon, vol. 167, pp. 559-574, 2020.

 doi:10.20944/preprints202509.2454.v1

42. C. Wan, H. Li, L. Zhao, Z. Li, C. Zhang, X. Tan, X. Liu, Mechanism of removal and degradation characteristics of dicamba by biochar prepared from Fe-modified sludge, J. Environ. Manage., 299, 113602, (2021).
43. Leng, L., Xu, S., Liu, R., Yu, T., Zhuo, X., Leng, S., ... & Huang, H. Nitrogen containing functional groups of biochar: An overview. Bioresource Technol., 298, 122286 (2020).
44. Jansen, R. J. J., & Van Bekkum, H.. XPS of nitrogen-containing functional groups on activated carbon. Carbon, 33, 1021-1027 (1995).
45. Q. Shi, X. Zhang, B. Shen, K. Ren, Y. Wang, J. Luo, Enhanced elemental mercury removal via chlorine-based hierarchically porous biochar with CaCO3 as template, Chem. Eng. J., 406, 126828, (2021).
46. Z. Song, T. F. Donald, W. Kirk, C. Q. Jia, Electrochemical Performance of Pre-Modified Birch Biochar Monolith Supercapacitors by Ferric Chloride and Ferric Citrate, Batteries, 11, 47, (2025).
47. Igor V. Esarev, D. V. Agafonov, Y. V. Surovikin, S. N. Nesov, A. V. Lavrenov, On the causes of non-linearity of galvanostatic charge curves of electrical double layer capacitors, Electrochim. Acta, 390, 138896, (2021).
48. M. Omidvar, S. Dalvand, A. Asghari, N. Yazdanfar, HY Sadat, N. Mohammadi, Fabrication of an efficient supercapacitor based on defective mesoporous carbon as electrode material utilizing Reactive Blue 15 as novel redox mediator for natural aqueous electrolyte, Fuel, 347, 128472, (2023).
49. B. A. Hemdan, D. A. Jadhav, A. Dutta, P. Goswami, Facilitating the electrochemical characterization and biofilm enrichment through anode modification in microbial fuel cells, J. Water Process Eng., 54, 104065, (2023).
50. Y. Lia, D. Zhang, Y. Zhang, J. He, Y. Wang, K. Wang, Y. Xu, H. Li, Yi Wang, Biomass-derived microporous carbon with large micropore size for high-performance supercapacitors, J. Power Sources, 448, 227396, (2020).
51. H. Noh, Y. Park, A. Bhadouria, B. M. Tackett, Effects of electrochemical active surface area of Cu on electrochemical CO reduction in acidic electrolyte using Cu nanoparticles on surfactant-treated carbon, J. Catalysis, 437, 115662, (2024).
52. Z. Ouyang, Y. Lei, Y. Chen, Z. Zhang, Z. Jiang, J. Hu, Y. Lin, Nanoscale Res. Lett. 14, 1–9 (2019)
53. S.A. Mousavianfard, A. Molaei, M. Manouchehri, A. Foroozandeh, A. Shahmohammadi, S. Dalvand, J. Energy Storage. 109, 115232 (2025).
54. Hsia, B., Kim, M. S., Carraro, C., & Maboudian, R. Cycling characteristics of high energy density, electrochemically activated porous-carbon supercapacitor electrodes in aqueous electrolytes. Journal of Materials Chemistry A, 1(35), 10518-10523 (2013). .
55. T. Zhu, F. Tian, J. Wu, H. Li, D. Chen, R. Qi, Y. Niu, F. Zhang, Z. Yang, Synthesis of various nanostructured N-doped Cu7S4 materials for aqueous supercapacitors, Electrochim. Acta, 511, 145396, (2025).
56. Wang, Z., Pan, S., Wang, B., Qi, J., Tang, L., & Liu, L. Asymmetric supercapacitors based on Co_3O_4@MnO_2@PPy porous pattern core-shell structure cathode materials. J. Electrochem. Sci. Technol. 12, 346-357 (2021).
57. Ye, Z., Wang, F., Jia, C., Mu, K., Yu, M., Lv, Y., & Shao, Z. Nitrogen and oxygen-codoped carbon nanospheres for excellent specific capacitance and cyclic stability supercapacitor electrodes. Chemical Engineering Journal, 330, 1166-1173 (2017).
58. W. Dong, M. Xie, S. Zhao, Q. Qin, F. Huang, Materials design and preparation for high energy density and high power density electrochemical supercapacitors, Mater. Sci. Eng., R., 152, 100713, (2023).
59. Z. Song, W. Liu, P. Xiao, Z. Zhao, G. Liu, J. Qiu, Nano-iron oxide (Fe_2O_3)/three-dimensional graphene aerogel composite as supercapacitor electrode materials with extremely wide working potential window, Mater. Lett., 145, 44-47, (2015).
60. F.-Y. Zeng, Z.-Y. Sui, S. Liu, H.-P. Liang, H.-H. Zhan, B.-H. Han, Nitrogen-doped carbon aerogels with high surface area for supercapacitors and gas adsorption, Mater. Today Commun., 16, 1-7, (2018).
61. G. A. Tafete, A. Uysal, N. G. Habtu, M. K. Abera, T. A. Yemata, K. S. Duba, S. Kinayyigit, Hydrothermally synthesized nitrogen-doped hydrochar from sawdust biomass for supercapacitor electrodes, Int. J. Electrochem. Sci., 19, 100827 (2024).
62. S. Rawat, T. Boobalan, B. B. Krishna, M. Sathish, S. Hotha, T. Bhaskar, Biochar for Supercapacitor Application: A Comparative Study, 17, e202200982, (2022).

 doi:10.20944/preprints202509.2454.v1

63. Z. Ma, H. Su, Y. Li, K. Yang, L. Dang, F. Li, B. Xue, Preparation of porous biochar and its application in supercapacitors, New J. Chem., 46, 21788-21797, (2022).
64. S. Nirmaladevi, R. Boopathiraja, S. K. Kandasamy, S. Sathishkumar, M. Parthibavarman, Wood based biochar supported MnO_2 nanorods for high energy asymmetric supercapacitor applications, Surf. Interfaces, 27, 101548, (2021).
65. C.-F. Xue, Y. Lin, W. Zhao, T. Wu, Y-Y. Wei, X.-H. Li, W.-J. Yan, X.-G. Hao, Green preparation of high active biochar with tetra-heteroatom self-doped surface for aqueous electrochemical supercapacitor with boosted energy density, J. Storage Mater., 90, 111872, (2024).
66. J. Cheng, Y. Lu, Y. Sun, S. Deng, H. Yang, M. Zhang, C. Wang, J. Yan, Impact of Activation Conditions on the Electrochemical Performance of Rice Straw Biochar for Supercapacitor Electrodes, Molecules, 30, 632, (2025).